ChemComm

COMMUNICATION

View Article Online
View Journal | View Issue

Cite this: *Chem. Commun.*, 2025, **61**, 18360

Received 1st September 2025,
Accepted 16th October 2025

DOI: 10.1039/d5cc05037e

rsc.li/chemcomm

Controllable growth of two dimensional stereoscopic $PtTe_2$ nanosheets for efficient electrocatalytic hydrogen evolution

Jiatian Fu,†[a] You Peng,†[b] Liang Zhou,[c] Jialong Wang,[a] Yahuan Huan,[a] Tong Zhou,[b] Haoxuan Ding,[a] Rongming Wang [c] and Yanfeng Zhang *[ab]

Among the transition metal dichalcogenide family, two-dimensional (2D) $PtTe_2$ has emerged as a promising electrocatalyst for the hydrogen evolution reaction (HER), due to its high edge catalytic activity, excellent conductivity and chemical stability, *etc.* However, the active sites of 2D $PtTe_2$ synthesized on conventional planar insulating substrates are limited to the edges, and the traditional synthetic method is not compatible with low-cost batch production. Herein, we report the large-area uniform growth of stereoscopic $PtTe_2$ nanosheets on highly conductive, carbon cloth substrates featuring abundant active sites and tunable thicknesses (from ~3.0 nm to bulk state), *via* a facile chemical vapor deposition route. We find that the stereoscopic structure of $PtTe_2$ on the carbon fiber surface can facilitate efficient electron transport from the conductive carbon cloth to the active edge sites of the $PtTe_2$ nanosheets along the in-plane direction. And the catalytic activity can be significantly improved by increasing the average nanosheet thickness from ~3.0 to 7.5 nm, leading to an ultra-low overpotential of ~38.8 mV at the current density of 10 mA cm^{-2} and a rather low Tafel slope of ~59.2 mV dec^{-1}. Hereby, this work is expected to deepen our understanding of the thickness-dependent catalytic activity of 2D layered materials, and stimulate further structure design and synthesis explorations of 2D catalysts on 3D templates for highly efficient water splitting related applications.

Among the huge transition metal dichalcogenide (TMDC) family, two-dimensional (2D) $PtTe_2$ has drawn tremendous attention, due to its unique properties (*e.g.*, type-II Dirac fermion,[1] excellent conductivity[2] and robust air stability[3]), and various applications in electrocatalysis,[4] terahertz emission, mid-infrared photodetection,[3] *etc.* As electrocatalysts in the hydrogen evolution reaction (HER), 2D $PtTe_2$ nanosheets exhibit high edge catalytic activities, due to the ultra-low hydrogen adsorption Gibbs free energy (~0.09 eV by theoretical calculations).[5] Intriguingly, distinguished from common TMDCs (*e.g.*, MoS_2[6] and ReS_2) with fewer *d*-electrons, the d orbitals of group-10 metal atoms were nearly fully occupied, and the p_z orbitals of interlayer chalcogen atoms of related TMDCs were highly hybridized. This resulted in strong interlayer interactions, and strong thickness-dependent electronic structures/properties.[7] The catalytic activity of group-10 metal related TMDCs should hereby correlate with their thicknesses and edge sites, since thicker flakes expose more catalytically active sites and exhibit tunable band gaps (even to zero). For example, $PtSe_2$ displays an exceptional bandgap transition (from ~1.28 to 0.23, and 0 eV) from monolayer to trilayer and bulk state,[8] enhanced conductivity from bilayer (~4×10^2 S m^{-1}) to twenty layers (~2×10^5 S m^{-1}),[9] and relatively high catalytic activities.[9]

Similarly, 2D $PtTe_2$ also displayed a semiconducting-to-metallic transition (bandgap ~0.5–0 eV) from monolayer to bilayer.[10] It crossed from a 2D metal to a three-dimensional (3D) type-II Dirac semimetal with increasing thicknesses from 2–3 to 4–6 layers, for molecular beam epitaxy (MBE) derived $PtTe_2$ films.[11] Besides affecting the electronic structure, the thickness of $PtTe_2$ also determines the loading amount of Pt, which makes identifying an optimal $PtTe_2$ nanosheet thickness crucial for maximizing the HER activity while reducing the noble metal usage. In addition, theoretical predictions revealed that the catalytically active sites of intrinsic 2D $PtTe_2$ for the HER were situated on the edges, while its basal plane was inert.[12] So far, $PtTe_2$ islands,[10] nanosheets[2] and thin films[3] have been achieved on 2D planar substrates (*e.g.*, 6H-SiC(0001), mica and SiO_2/Si) by MBE, CVD or thermal-assisted conversion routes.[13]

Compared with 2D planar nanosheets, catalysts with stereoscopic structures (*e.g.*, CoS_2 microwires or nanowire arrays and vertically-oriented MoS_2, TaS_2,[14] NbS_2[15] and $PtSe_2$[16] nanosheets) can expose more edge sites, facilitate the depinning and releasing of H_2 bubbles from the catalyst surfaces, and improve the overall

[a] *School of Materials Science and Engineering, Peking University, Beijing 100871, P. R. China. E-mail: yanfengzhang@pku.edu.cn*
[b] *Academy for Advanced Interdisciplinary Studies, School of Materials Science and Engineering, Peking University, Beijing 100871, P. R. China*
[c] *Beijing Advanced Innovation Center for Materials Genome Engineering, Beijing Key Laboratory for Magneto-Photoelectrical Composite and Interface Science, School of Mathematics and Physics, University of Science and Technology Beijing, Beijing 100083, P. R. China. E-mail: rmwang@ustb.edu.cn*
† These authors contributed equally.

HER performance. In addition, the stereoscopic structures can enable efficient electron transport from conductive substrates to the active edge sites of TMDCs along the in-plane direction, which can avoid the interlayer potential barrier effect.[14] Motivated by these results, we have designed a facile atmospheric-pressure CVD (APCVD) route to achieve the direct synthesis of stereoscopic $PtTe_2$ nanosheets with tunable thicknesses on low-cost, scalable, highly conductive carbon cloth (CC) substrates. Carbon fibers with highly curved surfaces were selected to induce high density nucleation, and the stereoscopic growth of 2D $PtTe_2$ nanosheets. A metal-precursor pre-coating strategy was developed to guarantee the uniform, controllable supply of metal precursor, thus enabling the uniform growth of stereoscopic $PtTe_2$ nanosheets, in line with the recent batch production of 2D materials. The achieved 3D hybrids were selected as perfect candidates to explore the thickness-dependent electrocatalytic properties in the HER. Overall, this work is envisioned to propel spatial structural design and performance improvement in $PtTe_2$-based catalysts.

The APCVD growth of 3D vertically-oriented 1T-TaS_2[14] and 1T-$PtSe_2$[16] nanosheets was realized by our group, by using nanoporous gold (NPG) as a substrate (Fig. S1, Fig. S2, SI). Herein, commercial carbon cloth (CC) is selected as the substrate for the growth of stereoscopic $PtTe_2$ nanosheets (Fig. 1a), since commercial CC is woven from carbon fibers (Fig. 1b), showing good conductivity, excellent thermal/chemical stability and low-cost, *etc.* Moreover, the 3D curved surfaces (Fig. 1c) can provide large surface areas, enabling stereoscopic nucleation and growth of $PtTe_2$ nanosheets (Fig. 1c and d). The uniform feeding of the metal precursor is also a key step, which was realized by dripping well-optimized $PtCl_2$/HCl solution onto the CC substrate followed by a drying process (Fig. 1e).

A facile APCVD route was then executed, by using Te powder as the precursor (Fig. S3, SI). After APCVD growth (Te precursor at ~650 °C), the chemical composition of the as-grown samples was first determined by X-ray photoelectron spectroscopy (XPS) (Fig. 1f). The Pt $4f_{7/2}$ and $4f_{5/2}$ peaks occur at binding energies of ~72.5 and ~75.8 eV, while the Te $3d_{5/2}$ and $3d_{3/2}$ peaks appear at ~573.2 and ~583.6 eV, respectively. These results agree well with the reported XPS spectra of mechanically exfoliated 1T-$PtTe_2$ flakes, confirming the successful synthesis of 1T-$PtTe_2$. Notably, the other two peaks at ~575.6 and 586.0 eV are assigned to Te–O bonds (Fig. S4, SI), possibly due to the formation of TeO_2 and its sub-oxide form (TeO_{2-x}).[3]

The volatilization temperature of the Te precursor was found to be an essential parameter for modulating the growth morphology of $PtTe_2$. The $PtCl_2$@CC with the $PtCl_2$ loading mass of ~0.8 mg cm^{-2} was first selected, under the same growth temperature of ~700 °C for ~15 min, but with different volatilization temperatures of Te. By gradually increasing the temperature of Te from ~500 °C, to ~550 °C, to ~600 °C, sparsely distributed $PtTe_2$ nanosheets (~30 nm in edge size) (Fig. 1g), high density irregular shaped flakes (~100 nm) (Fig. 1h), and regular shaped flakes (truncated triangles or hexagons) were obtained on the carbon fibers (Fig. S5, SI), respectively. At ~650 °C, the $PtTe_2$ nanosheets showed increased thickness to ~150 nm, and uniform truncated triangular or hexagonal shapes

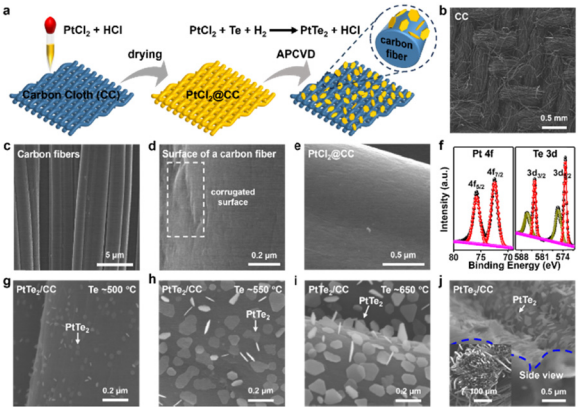

Fig. 1 APCVD growth of stereoscopic $PtTe_2$ nanosheets on the highly corrugated surfaces of carbon cloths (CCs) inner weaved by carbon fibers. (a) Schematic illustration of the synthesis strategy for stereoscopic $PtTe_2$ nanosheets on CC, by combining a facile metal precursor pre-coating strategy with a subsequent APCVD process. (b) Large-scale SEM image of the CC substrate. (c) SEM image of carbon fiber bunches. (d) SEM image of the corrugated carbon fiber surface. (e) SEM image of carbon fibers after being pre-coated with the $PtCl_2$ precursor (loading mass: ~0.8 mg cm^{-2}). (f) XPS spectra regarding Pt and Te elements for the as-grown samples (Te precursor at ~650 °C and $PtCl_2$ loading mass of ~0.8 mg cm^{-2}). (g)–(i) Representative SEM images of as-grown $PtTe_2$ nanosheets on carbon fibers ($PtCl_2$ loading mass of ~0.8 mg cm^{-2}) at different Te precursor temperatures of ~500 °C (c), 550 °C (d), and 650 °C (e), respectively. (j) Side-view SEM image of the as-grown $PtTe_2$ nanosheets on carbon fibers revealing their stereoscopic structures. Inset: Corresponding SEM image of the cut CC substrate with the blue curve indicating the cut edge.

(Fig. 1i). In addition, the contrasts of the $PtTe_2$ nanosheets gradually deepened with increasing Te temperature, indicating the increased nanosheet thicknesses, as similarly reported for the growth of few-layer WS_2 flakes.

According to the representative side-view SEM image, the $PtTe_2$ nanosheets were vertically or inclinedly grown on the highly curved surfaces of the carbon fibers, showing stereoscopic structures (Fig. 1j) (Fig. S6, SI). This growth behaviour is similar to the CVD growth of HfS_2 on SiO_2/Si[17] or VSe_2 on sapphire. The growth of $PtTe_2$ should follow the dangling-bond-assisted self-seeding growth mechanism. Altogether, under the uniform supply of metal precursor, an optimal Te precursor temperature (*i.e.*, ~650 °C) is crucial for achieving large-area uniform, stereoscopic $PtTe_2$ nanosheets with regular shapes on carbon fibers.

At the optimal Te temperature (~650 °C), the morphologies of $PtTe_2$ are investigated with varying loading mass of $PtCl_2$ precursor (from ~0.2 to 2.0 mg cm^{-2}). Notably, the $PtTe_2$ nanosheets present hardly changed flake sizes (Fig. 2a–c, ~150 nm), showing the unique stereoscopic configurations with truncated triangular or hexagonal shapes. Notably, similar nucleation densities (~35 nanosheets μm^{-2}) and large-scale uniform morphologies can be achieved (Fig. S6–S9, SI), possibly due to the uniform supply of metal precursor *via* the designed metal precursor pre-coating strategy. As reported previously, the in-plane (E_g) and out-of-plane (A_{1g}) modes of 2D $PtTe_2$

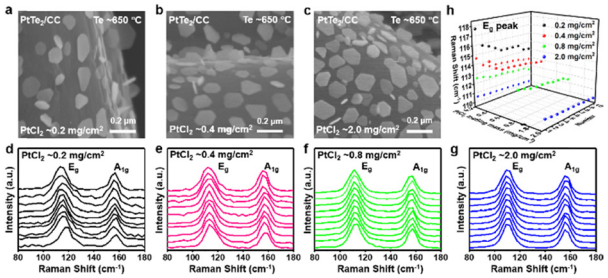

Fig. 2 Thickness-controllable growth and Raman characteristics of stereoscopic $PtTe_2$ nanosheets on carbon fibers (achieved by adjusting the loading mass of $PtCl_2$ precursor). (a)–(c) Representative SEM images of as-grown $PtTe_2$ nanosheets (with Te precursor hold at ~650 °C) under different $PtCl_2$ loading masses of ~0.2 (a), 0.4 (b), and 2.0 mg cm^{-2} (c), respectively. (d)–(g) Raman spectra captured from as-grown $PtTe_2$ nanosheets with different $PtCl_2$ loading masses of ~0.2 (d), 0.4 (e), 0.8 (f) and 2.0 mg cm^{-2} (g), respectively. (h) Corresponding statistical distribution of the E_g peak positions extracted from (d)–(g), showing a continuous redshift with increasing $PtCl_2$ loading, and average thickness evolution from ~3.0 to ≥12 nm.

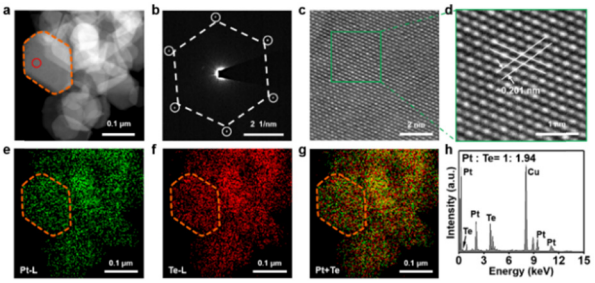

Fig. 3 Representative TEM and EDS characterizations of the $PtTe_2$ nanosheets after being transferred onto the Cu grid, showing the rather high crystal quality. (a) Low-magnification TEM image of the $PtTe_2$ nanosheets. (b) Corresponding SAED pattern captured from the red circle region in (a), indicating the single-crystal nature of the hexagonal-shaped $PtTe_2$ nanosheets. (c) Corresponding HR-TEM image (captured from the orange circle in (a)). (d) Zoomed-in HR-TEM image of the green square in (c), showing a lattice spacing of ~0.201 nm. (e)–(g) Corresponding EDS elemental mapping images regarding Pt and Te elements, and the mixture of Pt and Te captured from (a). (h) Corresponding EDS spectrum of the selected area in (e).

redshift with increasing thicknesses.[2] Herein, a series of Raman spectra were collected to extract the E_g peak positions (Fig. 2d-h) and average thickness of the $PtTe_2$ flakes. With increasing $PtCl_2$ loading amounts from ~0.2 to 0.4, 0.8, and 2.0 mg cm^{-2}, the E_g peaks redshift from ~117.7–114.2 cm^{-1} to 114.6–112.9, 112.6–111.6, and 110.5–110.2 cm^{-1}, corresponding to average thicknesses of ~3.0, 5.0, 7.5, and ≥12 nm, respectively (Fig. 2d–g).

In summary, by adjusting the $PtCl_2$ precursor amount, thickness-controlled growth of large-area uniform, stereoscopic $PtTe_2$ nanosheets can be achieved on CC substrates. When directly used as electrocatalysts in the HER, electron transport from the carbon fibers to the active edge sites can be realized through in-plane rather than from out-of-plane directions (needs to overcome the interlayer potential barrier). This enables 2D stereoscopic $PtTe_2$ nanosheets as perfect platforms in electrocatalytic related explorations.

High-resolution transmission electron microscopy (HR-TEM) and energy-dispersive X-ray spectroscopy (EDS) characterizations were then performed to examine the crystal quality and chemical composition of the CVD-derived $PtTe_2$ nanosheets. As shown in Fig. 3a, $PtTe_2$ nanosheets are distinguished in the low-magnification TEM image, presenting truncated triangular or hexagonal shapes. The stacked form arises from aggregation of nanosheets from the transfer process, due to the van der Waals interlayer interaction. The selected-area electron diffraction (SAED) pattern (Fig. 3b) presents a single set of diffraction spots with six-fold symmetry, suggesting the hexagonal crystal structure. Moreover, the HR-TEM image of the $PtTe_2$ nanosheets (Fig. 3c, d and Fig. S10 in SI) demonstrates a perfect lattice with a spacing of ~0.201 nm, consistent with the lattice spacing of the (110) plane of the 1T-$PtTe_2$ flakes.[2] Additional EDS mapping images confirm the large area uniform element ratio of Pt/Te ~1 : 1.94 (Fig. 3e–h). Overall, the CVD-derived stereoscopic $PtTe_2$ nanosheets possess a 1T-phase structure and high crystal quality.

Furthermore, the as-grown stereoscopic $PtTe_2$ nanosheets on CC substrates with different thicknesses are directly used for the electrocatalytic HER (schematic image in Fig. 4a). The polarization curves of the stereoscopic $PtTe_2$ nanosheets are displayed in Fig. 4b, with average thicknesses varying from ~3.0 nm ($PtCl_2$ ~0.2 mg cm^{-2}), 5.0 nm ($PtCl_2$ ~0.4 mg cm^{-2}), and 7.5 nm ($PtCl_2$ ~0.8 mg cm^{-2}) to the bulk state (≥12 nm) ($PtCl_2$ ~2.0 mg cm^{-2}). Notably, the overpotentials at the current density of 10 mA cm^{-2} (η_{10}) significantly decrease from ~65.6 to 48.5 to 38.8 mV (from ~3.0 nm to 5.0 nm to 7.5 nm), and the Tafel slopes (extracted from the linear portions of the

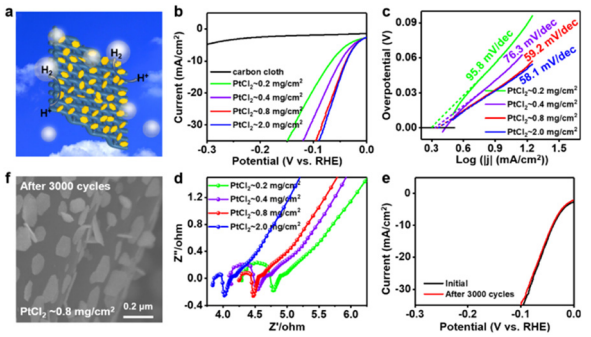

Fig. 4 Thickness-dependent catalytic activity of stereoscopic $PtTe_2$ nanosheets on CC substrates. (a) Schematic illustration of the HER process. (b) Polarization curves of stereoscopic $PtTe_2$ nanosheets with different thicknesses from ~3.0 nm ($PtCl_2$ ~0.2 mg cm^{-2}), to ~5.0 nm ($PtCl_2$ ~0.4 mg cm^{-2}), ~7.5 nm ($PtCl_2$ ~0.8 mg cm^{-2}) and bulk (≥12 nm) ($PtCl_2$ ~2.0 mg cm^{-2}), with the bare CC substrate as a reference. The η_{10} values are ~65.6, 48.5, 38.8 and 37.5 mV, respectively. (c) Corresponding Tafel plots of different samples in (b) showing Tafel slope values of ~95.8, 76.3, 59.2 and 58.1 mV dec^{-1}, respectively. (d) EIS Nyquist plots of different samples in (b). (e) Polarization curves of stereoscopic $PtTe_2$ nanosheets ($PtCl_2$ ~0.8 mg cm^{-2}, 7.5 nm thick) before and after 3000 cycles of CV tests. The overlapping curves confirm the robust stability of the catalyst. (f) SEM image of the stereoscopic $PtTe_2$ nanosheets (~7.5 nm thick) on a CC substrate after CV tests.

polarization curves) decrease accordingly from ~95.8 to 76.3 to 59.2 mV dec^{-1} (Fig. 4c). The exchange current density (J_0) (calculated by extrapolating the Tafel plot) (Fig. 4c) increases from ~2.0 to 2.17 to 2.29 mA cm^{-2}, possibly due to the increased active sites for the HER with increasing thicknesses. As a result, the catalytic activity of the stereoscopic $PtTe_2$ nanosheets can be enhanced with increasing the $PtTe_2$ thicknesses in a suitable range. Further electrochemical impedance spectroscopy (EIS) measurements were also performed to show the electrode kinetics (Fig. 4d), and the charge transfer resistances (R_{ct}) vary from ~0.46 to 0.38 to 0.18 Ω, accordingly. This indicates the faster electron transfer of the stereoscopic $PtTe_2$ on CC during the HER process.

However, with increasing the thickness from ~7.5 nm to bulk (≥12 nm), the η_{10}, Tafel slope, J_0 and R_{ct} values change a little from ~38.8 to 37.5 mV, from ~59.2 to 58.1 mV dec^{-1}, from ~2.29 to 2.32 mA cm^{-2}, and from ~0.18 to 0.16 Ω (Fig. 4b–d), respectively. This nearly stable catalytic property is possibly due to the limited exposure of active edge sites in thicker nanosheets (>7.5 nm). Additionally, the long-term stability of the stereoscopic $PtTe_2$ nanosheets is further evaluated by cyclic voltammetry (CV), which shows a negligible difference before and after 3000 cycles (Fig. 4e). And the $PtTe_2$ nanosheets maintain the initial morphology after the HER tests (Fig. 4f). A comparison of the HER performances of various TMDC-based catalysts is also performed (Table S1, SI). The stereoscopic 2D $PtTe_2$ nanosheets (~7.5 nm thick) exhibit superior catalytic properties to many reported 2D TMDC-related catalysts, and comparable to noble-metal-based electrocatalysts. As a result, the developed 2D stereoscopic $PtTe_2$ nanosheets on CC substrate systems can present relatively high electrocatalytic activity, low noble metal usage, excellent durability, facile production process, *etc.*

In summary, we have developed a facile APCVD route for the controllable growth of large-area uniform, thickness tunable stereoscopic $PtTe_2$ nanosheets on CC substrates. The thickness-dependent catalytic activity is unveiled to find ultrathin nanosheets with relatively high catalytic properties, while possessing low noble metal use amount. Notably, nanometer-thick, stereoscopic 3D $PtTe_2$ nanosheets can exhibit superior catalytic properties to many 2D TMDC catalysts, and comparable properties to noble-metal-based catalysts, showing the advantages of relatively high electrocatalytic activity, low noble metal usage, excellent durability, and facile production process, *etc.* Briefly, this catalytic system can serve as a practical model for examining the thickness-dependent catalytic activity, the internal mechanism and the property modulation of group-10 metal-related TMDCs. This work should promote the direct synthesis and application exploration of related catalysts in various energy related fields.

This work was financially supported by the National Natural Science Foundation of China (No. 92477204, T2188101, and 52021006) and Xianyang Science and Technology Bureau (Project L2024-ZDKJ-ZDCGZH-0009 and Project L2024-ZDYF-ZDYF-GY-0013).

Conflicts of interest

There are no conflicts to declare.

Data availability

Data supporting this article are available in the supplementary information (SI). Supplementary information: details of experimental information, supporting SEM images, TEM images and electrochemical measurements. See DOI: **https://doi.org/10.1039/d5cc05037e**.

Notes and references

1 M. Yan, H. Huang, K. Zhang, E. Wang, W. Yao, K. Deng, G. Wan, H. Zhang, M. Arita, H. Yang, Z. Sun, H. Yao, Y. Wu, S. Fan, W. Duan and S. Zhou, *Nat. Commun.*, 2017, **8**, 257.
2 H. Ma, P. Chen, B. Li, J. Li, R. Ai, Z. Zhang, G. Sun, K. Yao, Z. Lin, B. Zhao, R. Wu, X. Tang, X. Duan and X. Duan, *Nano Lett.*, 2018, **18**, 3523–3529.
3 L. Zeng, D. Wu, J. Jie, X. Ren, X. Hu, S. P. Lau, Y. Chai and Y. H. Tsang, *Adv. Mater.*, 2020, **32**, 2004412.
4 W. Zhao, C. Cui, Y. Xu, Q. Liu, Y. Zhang, Z. Zhang, S. Lu, Z. Rong, X. Li, Y. Fang and W. Huang, *Adv. Mater.*, 2023, **35**, 2301593.
5 J. Chen, M. Qin, S. Ma, R. Fan, X. Zheng, S. Mao, C. Chen and Y. Wang, *Appl. Catal., B*, 2021, **299**, 120640.
6 Y. Wang, W. Zhai, Y. Ren, Q. Zhang, Y. Yao, S. Li, Q. Yang, X. Zhou, Z. Li, B. Chi, J. Liang, Z. He, L. Gu and H. Zhang, *Adv. Mater.*, 2023, 2307269.
7 Y. Zhao, J. Qiao, P. Yu, Z. Hu, Z. Lin, S. P. Lau, Z. Liu, W. Ji and Y. Chai, *Adv. Mater.*, 2016, **28**, 2399–2407.
8 J. Shi, Q. Ji, Z. Liu and Y. Zhang, *Adv. Energy Mater.*, 2016, **6**, 1600459.
9 D. Hu, T. Zhao, X. Ping, H. Zheng, L. Xing, X. Liu, J. Zheng, L. Sun, L. Gu, C. Tao, D. Wang and L. Jiao, *Angew. Chem., Int. Ed.*, 2019, **58**, 6977–6981.
10 J. Li, S. Kolekar, M. Ghorbani-Asl, T. Lehnert, J. Biskupek, U. Kaiser, A. V. Krasheninnikov and M. Batzill, *ACS Nano*, 2021, **15**, 13249–13259.
11 K. Deng, M. Yan, C.-P. Yu, J. Li, X. Zhou, K. Zhang, Y. Zhao, K. Miyamoto, T. Okuda, W. Duan, Y. Wu, X. Zhong and S. Zhou, *Sci. Bull.*, 2019, **64**, 1044–1048.
12 X. Xu, X. Wang, S. Yu, C. Wang, G. Liu, H. Li, J. Yang, J. Li, T. Sun, X. Hai, L. Li, X. Liu, Y. Zhang, W. Zhang, Q. Zhang, K. Wang, N. Xu, Y. Ma, F. Ming, P. Cui, J. Lu, Z. Zhang and X. Xiao, *ACS Nano*, 2024, **18**, 32635–32649.
13 F. Liu, Y. Hu, Z. Qu, X. Ma, Z. Li, R. Zhu, Y. Yan, B. Wen, Q. Ma, M. Liu, S. Zhao, Z. Fan, J. Zeng, M. Liu, Z. Jin and Z. Lin, *Proc. Natl. Acad. Sci. U. S. A.*, 2023, **120** (26), e2303262120.
14 Y. Huan, J. Shi, X. Zou, Y. Gong, Z. Zhang, M. Li, L. Zhao, R. Xu, S. Jiang, X. Zhou, M. Hong, C. Xie, H. Li, X. Lang, Q. Zhang, L. Gu, X. Yan and Y. Zhang, *Adv. Mater.*, 2018, **30**, 1705916.
15 Y. Peng, L. Zhu, C. Li, J. Hu, Y. Lu, J. Fu, F. Cui, X. Wang, A. Cao, Q. Ji, Y. Huan and Y. Zhang, *Adv. Energy Mater.*, 2024, **14**, 2302510.
16 K. Chen, Y. Huan, W. Quan, L. Zhu, J. Fu, J. Hu, F. Cui, F. Zhou, X. Wang, M. Li and Y. Zhang, *ACS Energy Lett.*, 2022, **7**, 3675–3684.
17 B. Zheng, Y. Chen, Z. Wang, F. Qi, Z. Huang, X. Hao, P. Li, W. Zhang and Y. Li, *2D Mater.*, 2016, **3**, 035024.